Reduced interface spin polarization by antiferromagnetically coupled Mn segregated to the Co_2MnSi/GaAs (001) interface

Ashutosh Rath,[1] Chockalingam Sivakumar,[2] C. Sun,[1] Sahil J. Patel,[3] Jong Seok Jeong,[4] J. Feng,[1] G. Stecklein,[5] Paul A. Crowell,[5] Chris J. Palmstrøm,[3] William H. Butler,[2] and Paul M. Voyles[1,*]

[1]*Department of Material Science and Engineering, University of Wisconsin-Madison, Madison, Wisconsin, USA*
[2]*Department of Physics & Astronomy, and Center for Materials for Information Technology, University of Alabama, Tuscaloosa, Alabama, USA*
[3]*Department of Materials Science and Engineering, University of California-Santa Barbara, Santa Barbara, California, USA*
[4]*Departments of Chemical Engineering and Materials Science, University of Minnesota, Minneapolis, Minnesota, USA,*
[5]*School of Physics and Astronomy, University of Minnesota, Minneapolis, Minnesota, USA*

(Received 27 June 2017; revised manuscript received 15 December 2017; published 22 January 2018)

We have investigated the interfacial structure and its correlation with the calculated spin polarization in Co_2MnSi/GaAs(001) lateral spin valves. Co_2MnSi (CMS) films were grown on As-terminated c(4×4) GaAs(100) by molecular beam epitaxy using different first atomic layers: MnSi, Co, and Mn. Atomically resolved Z-contrast scanning transmission electron microscopy (STEM) imaging and electron energy loss spectroscopy (EELS) were used to develop atomic structural models of the CMS/GaAs interfaces that were used as inputs for first-principles calculations to understand the magnetic and electronic properties of the interface. First-principles structures were relaxed and then validated by comparing experimental and simulated high-resolution STEM images. STEM-EELS results show that all three films have similar six atomic layer thick, Mn- and As-rich multilayer interfaces. However, the Co-initiated interface contains a Mn_2As-like layer, which is antiferromagnetic, and which is not present in the other two interfaces. Density functional theory calculations show a higher degree of interface spin polarization in the Mn- and MnSi-initiated cases, compared to the Co-initiated case, although none of the interfaces are half-metallic. The loss of half-metallicity is attributed, at least in part, to the segregation of Mn at the interface, which leads to the formation of interface states. The implications for the performance of lateral spin valves based on these interfaces are discussed briefly.

DOI: 10.1103/PhysRevB.97.045304

I. INTRODUCTION

Unlike conventional electronic devices, spintronic devices are based on the manipulation of the spin degree of freedom of electrons [1–3]. Adding the spin degree of freedom to conventional semiconductor charge-based electronics could offer many advantages such as nonvolatility, high speed data processing, ultralow power consumption and high integration densities [2–8]. Various spintronic devices require injection, transport, and manipulation of spin-polarized carriers in semiconductor heterostructures. A key parameter that determines the efficiency of most semiconductor spin-based devices is the degree of spin polarization in the semiconductor. Starting with a half-metallic ferromagnet electrode with 100% spin polarization at the Fermi level would be optimal for achieving high spin injection [9]. A variety of ferromagnetic Heusler alloys, such as Co_2MnSi, and Co_2MnGe are predicted to be half-metallic in the fully ordered crystal structure [10–12]. These full Heusler alloys are described by the chemical formula X_2YZ with X and Y typically being transition metals and Z being a group III, group IV, or group V element. Half Heusler alloys with the composition XYZ have also been predicted to exhibit half-metallicity [13], with experimental evidence existing for the case of NiMnSb [14].

Among the ferromagnetic full-Heusler alloys, Co_2MnSi(CMS) has attracted strong interest [11,15–24] due to its predicted large minority spin band gap of ~0.4 eV at the Fermi level [11] and high Curie temperature of 985 K [18]. Measurements of the bulk spin polarization range from 54% [21] to 60% [19] to 93% [23] using various techniques and materials [25]. CMS is also well-suited to devices, because it is lattice matched to GaAs semiconductor channels and MgO tunnel barriers. Estimates of the interfacial spin polarization in various devices range up to 89% at low temperature [20], with lower and widely varying values reported at room temperature [21,22,24,26,27].

A key question for spintronic applications of CMS and other Heuslers is whether or not they maintain their attractive magnetic properties at interfaces. In early work, Wang *et al.* grew CMS films on GaAs(001) substrates, and their spin-resolved photoemission measurements revealed not more than 12% spin polarization at the Fermi energy, in contrast to the predicted half-metallic behavior [24]. This large discrepancy was attributed to atomic disorder in the CMS lattice due to a chemical reaction at the GaAs interface. More recently, several groups have synthesized CMS thin films on GaAs and incorporated them into spintronic devices [14,26–29]. They, too, find that CMS does not exhibit 100% spin polarization at

*paul.voyles@wisc.edu

 ©2018 American Physical Society

the Fermi energy (as inferred from polarization of a tunneling current) when incorporated into heterostructures. The reason might be deterioration of half-metallicity in the vicinity of the boundary with the semiconductor. In-diffusion of Mn into the GaAs also can affect the spin injection, as Mn is reactive on a GaAs surface [30] and tends to replace the Ga-As bond with Mn-As [31], which affects the spin polarization. In addition, the change in periodicity and bonding due to the interface between the electrode and the channel causes the formation of interfacial states [32].

To understand the interfacial electronic and magnetic states, it is essential to determine the detailed atomic-scale structure of the CMS/GaAs interface and connect it to the magnetic properties through first-principle calculations. A few theoretical studies have addressed the problem of spin polarization at abrupt interfaces between a full-Heusler and a semiconductor [12,33,34]. The structural properties of CMS and how they affect the spin polarization have been studied in detail by first-principles calculations [5,32,35–39]. Recently, Nedelkoski *et al.* studied the effect of a CMS/Ag interface on the interface spin polarization using density functional theory (DFT) calculations based on an experimentally derived interfacial model [40]. Hashemifar *et al.* performed DFT calculations on the (001) surface of CMS to study the effect of different surface terminations on half-metallicity. They showed that MnSi-, Mn- and Si-terminated surfaces were more thermodynamically stable than Co-terminated surfaces and that Mn-terminated surfaces preserved half-metallicity [41]. In reality, the CMS/GaAs interfaces are more complicated than these idealized abrupt terminations due to solid-state reactions at the interface [42]. Thus it is essential for theoretical studies to obtain the true atomic configuration of the CMS/GaAs interface based on experiments and to relate the results to actual device performance.

Here, we investigate the interfacial structure of CMS/GaAs (001) heterostructures grown by molecular beam epitaxy. The films were deposited using a shuttered growth sequence for the first 10 monolayers of the CMS film to control the CMS/GaAs interfacial layer by deposition. Three types of samples were grown with three different interfacial layers: Co-initiated, MnSi-initiated, and Mn-initiated. The interfaces of these structures were studied using atomic-resolution electron microscopy and DFT calculations. Z-contrast scanning transmission electron microscopy (STEM) imaging is used to derive atom positions at the interface, and atomically resolved STEM and electron energy loss spectroscopy (EELS) mapping analysis on Co-, Mn-, Ga-, and As -$L_{2,3}$ edges is used to determine the elements occupying each interface site. The interface structural models derived from EELS have been used as inputs for first-principle calculations to understand the magnetic and electronic properties of the CMS/GaAs interface. The calculated structure and properties of these interfaces are then correlated to spin injection properties, although they do not provide a comprehensive picture of device performance.

II. EXPERIMENTAL AND COMPUTATIONAL DETAILS

The CMS layers were grown on As-terminated c(4×4) GaAs (100) at 270 °C by molecular beam epitaxy using different compositions of the first monolayer(ML): MnSi, Co, and Mn. The interface compositions were controlled using a shuttered ML by ML growth sequence for the first 10 monolayers of Co_2MnSi films, followed by Co, Mn, and Si codeposition with elementally calibrated fluxes for a total film thickness of 5 nm. The first monolayer was controlled by using a either a CoCo-MnSi-CoCo-MnSi sequence or a MnSi-CoCo-MnSi-CoCo sequence, where CoCo means 1ML of Co and MnSi means a total of 1 ML of Mn+Si. For a third sample structure, the first monolayer of MnSi was replaced by a full monolayer of Mn, corresponding to a sequence of MnMn-CoCo-MnSi-CoCo-.

Electron transparent cross-sectional transmission electron microscopy (TEM) samples were prepared by *in situ* lift out using a Zeiss Auriga focused ion beam (FIB). To minimize damage from implanted Ga, the samples were exposed to Ga ion beam energy of 5 kV or less after lift-out, and final FIB thinning was performed at 2 kV. The c(4×4) reconstruction of the GaAs surface consists of a complete As layer covered by rows of three As dimers along [110], separated by vacant As sites [43]. Thus, to determine the interface structure of the film grown on the c(4×4) surface requires two projections of the interface, one along [110], parallel to the dimer rows, and the other along [$1\bar{1}0$], perpendicular to the dimer rows. Two TEM samples were prepared for each sample, one oriented along the [110] zone axis of the GaAs, the other along [$1\bar{1}0$].

STEM imaging was performed on an FEI Titan STEM with a CEOS probe aberration corrector operated at 200 keV and 24.5 mrad convergence angle. Z-contrast images were collected with a detector spanning 54 to 270 mrad in scattering angle. EELS spectrum imaging was performed on another FEI Titan monochromated STEM with CEOS DCOR probe aberration corrector operated at 200 keV and equipped with an Enfinium ER EEL spectrometer. STEM-EELS composition maps were acquired simultaneously with annular dark-field (ADF)-STEM images. For EELS, the probe convergence angle was 17 mrad, the collection angle was 26 mrad, and the energy dispersion was 0.05 eV/channel. The energy resolution measured using the full width at half maximum (FWHM) of the zero-loss peak was 0.8 eV, and the measured probe size was 0.8 Å. EELS elemental maps of Mn -L_3 edge (640 eV), Ga -L_3 edge (1115 eV), Co-L_3 edge (779 eV), and As-L_3 edge (1323 eV) are extracted from the spectrum using standard power-law background subtraction [44] in DIGITAL MICROGRAPH software. We are not able to get the elemental map of Si-L edge (99.2 eV) due to the very small signal in EELS. The Si L-edge signal is suppressed by probe channeling effects in zone-axis oriented CMS [45].

Lateral spin valves with source and detection electrodes were fabricated from the three heterostructures using standard photolithography and etching techniques described elsewhere [28]. Nonlocal spin valve measurements were carried out using the biased-detector technique [28]. The magnetic field was swept in the plane, and the size of the nonlocal signal was determined from the difference in nonlocal voltages obtained when the source and detection electrodes were parallel and antiparallel.

We performed first-principles calculations based on DFT [46] using the generalized gradient approximation to the exchange-correlation functional [47], as implemented in the

Vienna *ab initio* simulations program [48–51]. For optimization of atomic coordinates, the conjugate-gradient algorithm was used [52]. Co_2MnSi/GaAs (001) complex interfaces for the three initiations (MnSi, Mn, and Co) were modeled in a periodic supercell. The two (identical) interfaces within the supercell were constructed by using the STEM and EELS mapping data to determine the initial physical structure and chemical composition. Several possible models based on this information were modeled with and without the presence of Si inside the interface, due to the fact that Si was difficult to map experimentally.

The supercells are tetragonal unit cells with square bases. The in-plane lattice parameter of the cell was set to the experimental lattice constant of GaAs, such that $a = b = a_{\text{exp}}/\sqrt{2}$, where $a_{\text{exp}} = 5.65$ Å. The lattice parameter along the direction perpendicular to the interface (c-parameter) was optimized. The super cell consisted of 11 layers of GaAs, 9 layers of CMS, and the complex interface simulated on both sides of the hetero junction, with a total of 49 ions in the supercell in case of MnSi initiation. Plane-wave basis sets with cutoff energy of 357 eV were used for self-consistent field calculations. The integration in the irreducible wedge of the supercell Brillouin zone was performed using a (12, 12, 1) k-point mesh with 49 k points, according to the Monkhorst-Pack scheme [53].

Frozen phonon simulations of the Z-contrast STEM images were performed using the Kirkland implementation [54] and a 52.2 Å × 45.9 Å × 405.5 Å GaAs-Co_2MnSi interface model, which was built from the static interface structure super cell fully relaxed by DFT. In the frozen phonon simulations, the model was sampled with a 2048 × 2048 pixel wave function and 16 phonon configurations were used. The simulated images were convolved with the 86.3 pm FWHM Gaussian function to account for incoherent source broadening [55]. All microscope settings are the same as the imaging experiments.

III. RESULTS AND DISCUSSION

A. Structural properties

Figure 1(a) shows a cross-sectional high-resolution high-angle ADF (HAADF)-STEM image of the MnSi-initiated CMS film deposited on the GaAs(001) surface taken along the [1$\bar{1}$0] zone axis of GaAs substrate. The epitaxial relationship is (001) CMS // (001) GaAs: [1$\bar{1}$0] CMS // [1$\bar{1}$0] GaAs, so the CMS is viewed also along the [1$\bar{1}$0] zone axis. The thickness of the CMS film is 5 nm and it is fully epitaxial. The interface is atomically flat, smooth and abrupt. The top of the film is in the ordered $L2_1$ structure, as shown by the intensity line profiles (inset figure) and the fast-Fourier transform (FFT) of the high-resolution image in Fig. 1(b). The intensity profile of the Co and MnSi layers (inset figure) along the [1$\bar{1}$0] direction of the CMS show consistent intensity for all the atomic columns in the Co layer and periodic intensity variation for the atomic columns in the MnSi layer, as expected for the $L2_1$ phase. The (111) spots are specific to the $L2_1$ structure, while the (002) spots occur in both the B_2 and $L2_1$ structures [56]. The (220) spots are the fundamental reflections. Closer to the interface, the film is in the B_2 phase, with disorder of the Mn and Si sites, as shown by the FFT in Fig. 1(c), which does not show the (111) reflections.

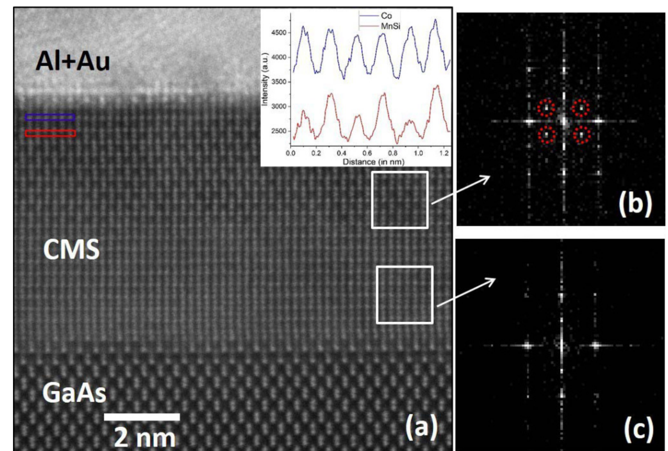

FIG. 1. (a) Cross-sectional high-resolution HAADF-STEM image of CMS film on GaAs(001) surface taken along the [1$\bar{1}$0] zone axis of a GaAs substrate and the line profile of Co and MnSi (inset figures), (b) and (c) shows the FFT of the region mentioned in (a), which indicates the $L2_1$ and B_2 phases, respectively.

Figures 2(a) and 2(h) show cross-sectional high resolution HAADF-STEM images of the CMS /GaAs interface for the MnSi-initiated sample taken along the [110] and [1$\bar{1}$0] zone axes of the GaAs substrate respectively. In order to determine the elemental distributions at the interface, EELS maps were observed from the area (red rectangle) shown in Figs. 2(a) and 2(h). Atomic resolution EELS maps of Mn, Co, Ga, and As are shown in Figs. 2(c), 2(d), 2(e), and 2(f), respectively. Figures 2(b) and 2(i) show the ADF-STEM images taken in parallel with the maps. By comparing the ADF image and elemental maps, we assign compositions to the atomic columns in the interface as shown in Fig. 2(g), with Mn in red, Co in blue, Ga in yellow and As in green (The same color scheme is followed throughout unless otherwise stated). Similarly, Figs. 2(i)–2(n) show the ADF image, color maps and atomic column assignments for [1$\bar{1}$0] direction. The red oval represents Mn atomic columns that are unresolved in the two dimensional projection of the STEM images. Si is not assigned to any sites as it is not detected in the EEL SIs. Figure 3 and 4 shows the same data as Fig. 2 but for the Mn- and Co-initiated samples, respectively.

Mn (Fig. 2) and MnSi (Fig. 3) both show complex, multilayer interfaces. The structures look identical, although the distribution of Si atoms could be different, since Si was not detected in EELS and is low scattering in Z-contrast STEM. The interfaces are six atomic layers thick, with significant As inside the first layer of the CMS. There is a partial occupancy of Mn in the last layer of GaAs. The intervening layers are Mn- and As-rich. Atoms are closely packed in all but one of the interfacial layers. There may be a vacancy in this intermediate interfacial layer or Si may be present in this layer, which cannot be confirmed due to the absence of EELS mapping of Si. The Co-initiated films (Fig. 4) also have Mn- and As-rich interfaces with a thickness of six atomic layers, but there is no partial occupancy of Mn in the last GaAs layer, and the distribution of Mn and As in the intervening layers is different compared to the previous films.

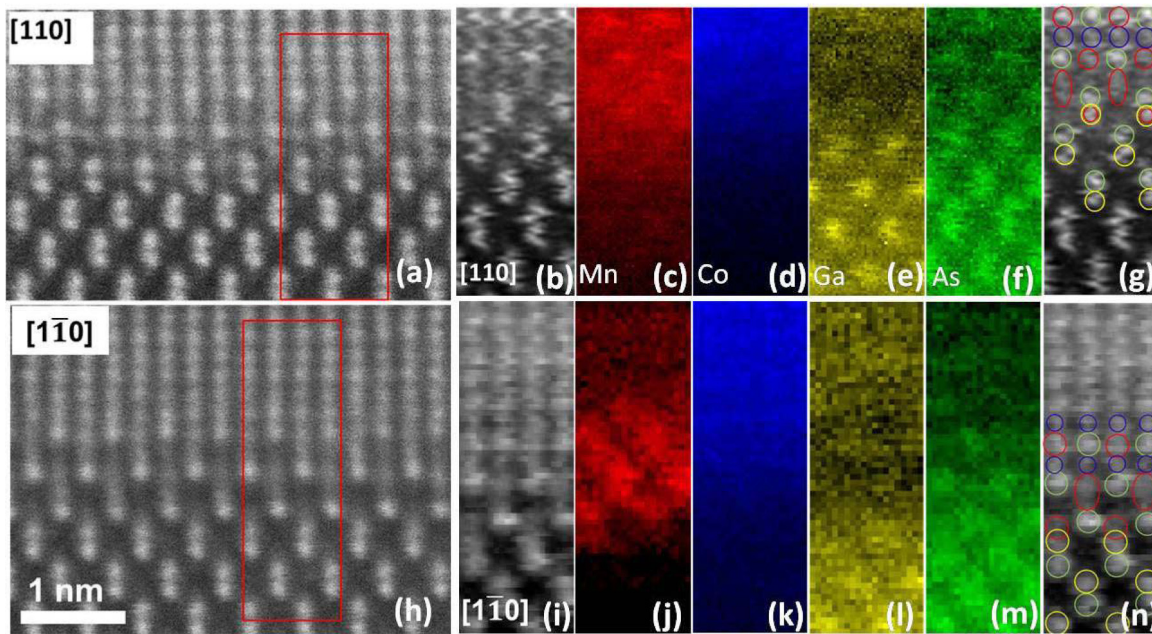

FIG. 2. (a) HAADF-STEM image of the CMS/GaAs interface for the MnSi initiated sample along the [110] direction (the red box outlines the location of the EELS maps). (b) ADF image taken in parallel with EELS map. (c)–(f) Atomic resolution EELS map of Mn (red), Co (blue), Ga (yellow), and As (green). (g) Model image after comparison of the EELS map and ADF image. Similarly, (h) HAADF-STEM image along the [1$\bar{1}$0] direction and corresponding EELS maps, ADF images, and model figure are shown in (i), (j), (k), (l), (m), and (n), respectively.

Figures 5 and 6 show our best DFT models of the Mn and MnSi initiated interfaces which appear to be identical experimentally. Figure 5(a) shows the ball-and-stick representation of the interfacial structure along the [110] direction, and Fig. 5(d) shows the projection along the [1$\bar{1}$0] direction. Yellow lines separate the interfacial structure from bulk GaAs (below the interface) and bulk CMS (above the interface). The six interface layers are labeled from L1 to L6 and the atoms are color coded (Co - blue, Mn - red, Si - turquois, As - green, and Ga - yellow). Layer L1 is the first layer of the interface after the bulk GaAs.

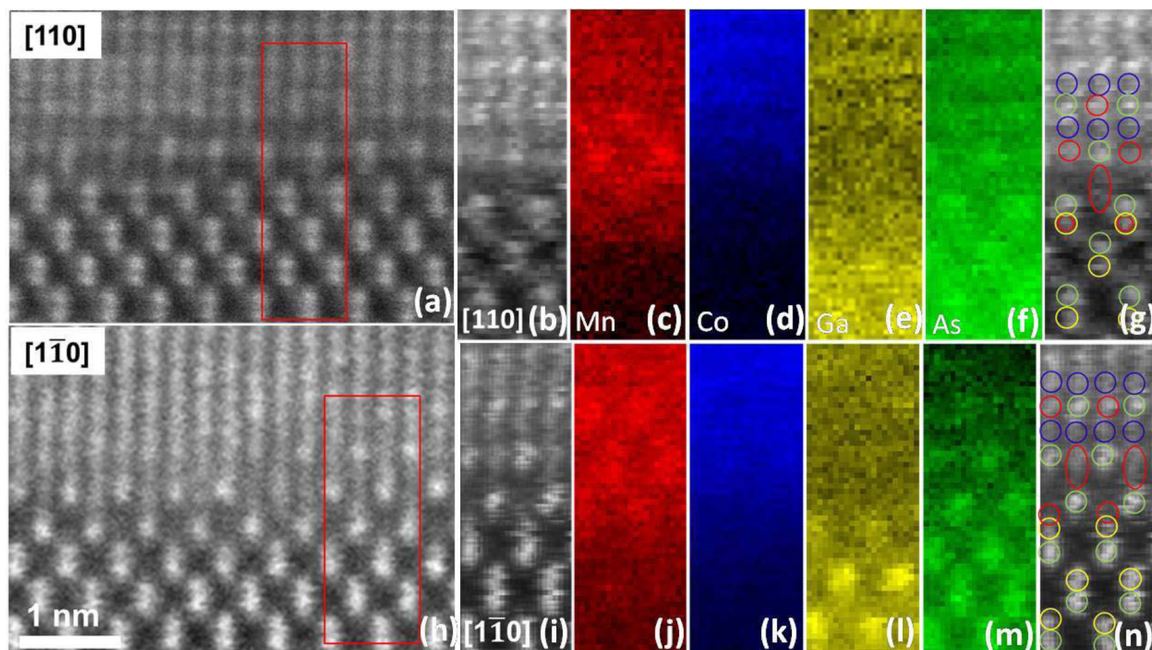

FIG. 3. (a) HAADF-STEM image of the CMS/GaAs interface for the Mn-initiated sample along the [110] direction (the red box outlines the location of the EELS maps). (b) ADF image taken in parallel with EELS map. (c)–(f) Atomic resolution EELS map of Mn (red), Co (blue), Ga (yellow), and As (green). (g) Model image after comparison of the EELS map and ADF image. Similarly, (h) HAADF-STEM image along the [1$\bar{1}$0] direction and corresponding EELS maps, ADF images and model figure are shown in (i), (j), (k), (l), (m), and (n), respectively.

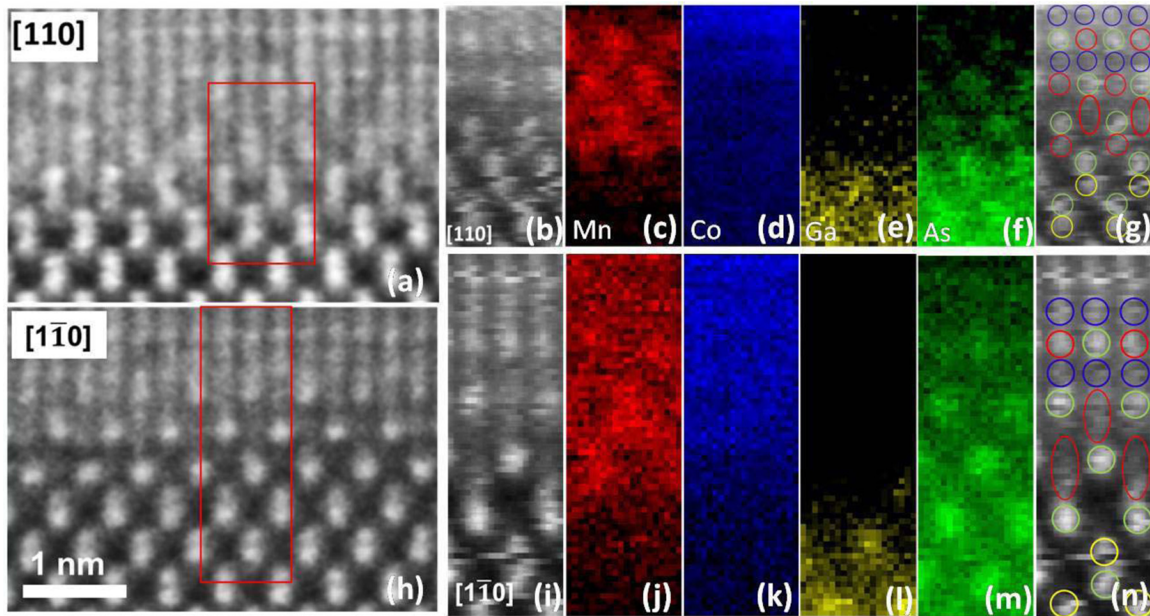

FIG. 4. (a) HAADF-STEM image of the CMS/GaAs interface for the Co-initiated sample along the [110] direction (the red box outlines the location of the EELS maps). (b) ADF image taken in parallel with EELS map. (c)–(f) Atomic resolution EELS map of Mn (red), Co (blue), Ga (yellow), and As (green). (g) Model image after comparison of the EELS map and ADF image. Similarly, (h) HAADF-STEM image along the [1$\bar{1}$0] direction and corresponding EELS maps, ADF images and model figure are shown in (i), (j), (k), (l), (m), and (n), respectively.

This layer is composed of Ga atoms. Layer L2 is comprised of Mn and As atoms. Layer L3 is composed of Mn and Si atoms. The Si atoms occupy low-intensity sites in the STEM image and vacant sites in the EELS composition maps. Layer L4 is composed of Mn and As atoms, and layer L5 is composed of Co atoms. Layer L6 is composed of Mn and As atoms, and is the last layer of the interface. In the model, $L2_1$ phase CMS atoms immediately follow layer L6.

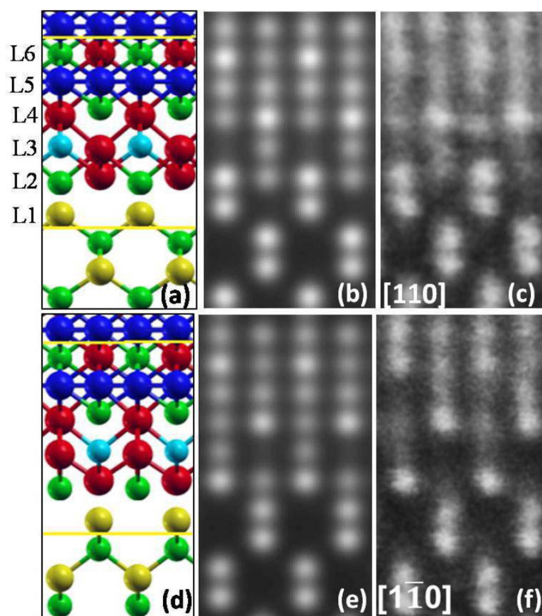

FIG. 5. (a) and (d) Ball-and-stick representation of the DFT-relaxed interface structure for the MnSi initiated model with Si at L3 along the [110] and [1$\bar{1}$0] directions, and (b) and (e) corresponding frozen-phonon multislice STEM simulations image. (c) and (f) High-resolution Z-contrast STEM images of the CMS/GaAs interface (MnSi initiated sample). Color scheme: Co - blue, Mn - red, Si - turquois, As - green, and Ga - yellow.

The Mn atom in L2 has Si (in L3) and Mn (in L3) as its nearest neighbors. The Si atom in L3 has Mn in L4 as its next nearest neighbor. While the Ga atom in L1 and As atom in L2 follow the zinc-blende pattern of GaAs, the bond-length between L1-Ga and L2-As is stretched by 12 pm, compared to the bond-length in bulk GaAs of 244 pm. There is one layer of Co inside the complex interface (at L5) with a layer of MnAs above and below it (L6 and L4), forming a Co_2MnAs-like structure. There is no formation of a Mn_2As-like interface pattern in layers 2–4 (L2–L4), due to the presence of Si in layer L3.

Figure 5 also shows simulated STEM images from the models [(b) and (e)] and equivalent sections of the experimental images of the MnSi-initiated sample for comparison [(c) and (f)]. The simulated images are in good agreement with the experimental images. They also look very similar to the STEM image of the Mn-initiated sample, since the interfacial structure for MnSi- and Mn-initiated samples look identical (see Figs. 2 and 3). The Z-contrast image intensity for Si atom in layer L3 is very weak compared to a relatively high-Z atom like As or Ga.

Figure 6 shows an alternate model of the Mn/MnSi interface with vacancies in place of Si in layer L3. The interface is six layers thick, with Mn diffusing inside the GaAs surface, pushing As above, at least three layers into the CMS alloy. The Mn atom at L2 is nearer to L1-Ga than L2-As. While the Ga atom in L1 and the As atom in L2 follow the zinc-blende pattern of GaAs, the bond-length between the L1-Ga and the L2-As is stretched by 20 pm, instead of 11 pm as in the Si-containing

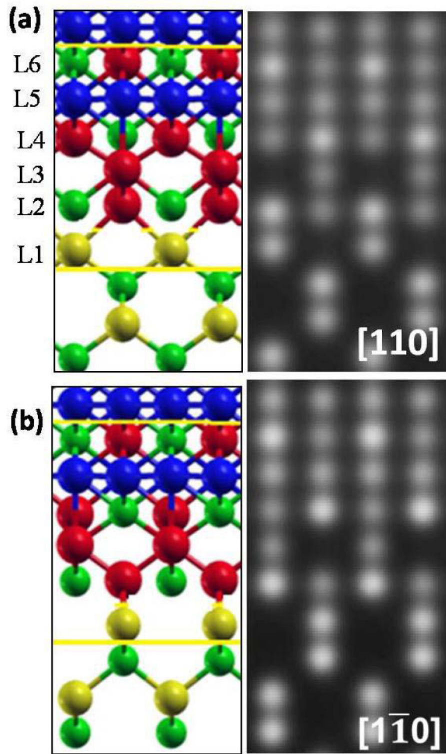

FIG. 6. Ball-and-stick representation of the DFT-relaxed interface structure for the MnSi-initiated interface without Si at L3 along the [110] (a) and [1$\bar{1}$0] (b) directions (left images), and corresponding frozen-phonon multislice STEM simulations image (right images), Color scheme: Co - blue, Mn - red, As - green, and Ga - yellow.

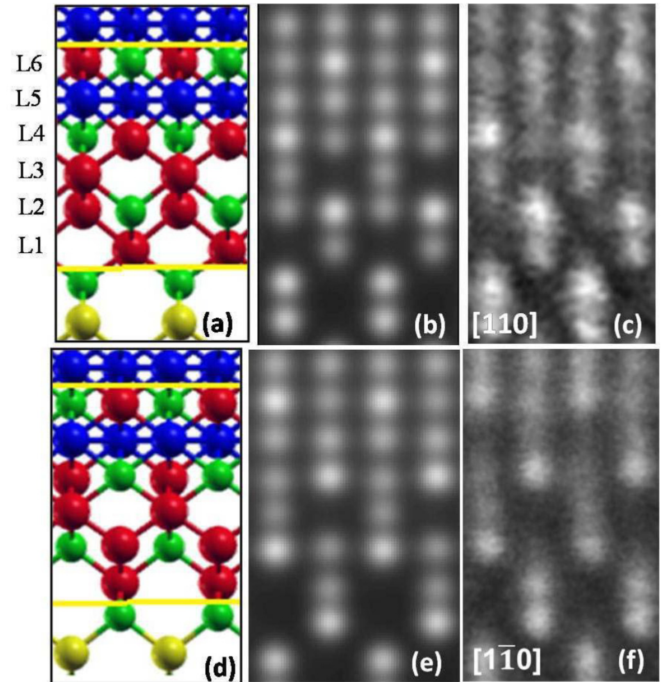

FIG. 7. (a) and (d) Ball-and-stick representation of the DFT-relaxed interface structure for the Co-initiated model along the [110] and [1$\bar{1}$0] directions, and (b) and (e) corresponding frozen-phonon multislice STEM simulations image. (c) and (f) High-resolution Z-contrast STEM images of the CMS/GaAs interface (Co-initiated sample).Color scheme: Co - blue, Mn - red, As - green, and Ga - yellow.

model. In addition, interface layers L2-L4 form a Mn_2As-like pattern. There is one layer of Co inside the complex interface (at L5) with a layer of MnAs above and below it (L6 and L4), forming a Co_2MnAs-like structure.

Both of the models in Figs. 5 and 6 are metastable, in the sense that Mn is expected to be incorporated into the bulk GaAs in thermodynamic equilibrium. The energy difference between the structures of Figs. 5 and 6 after allowing for the reference energy of the additional two Si atoms in the structure of Fig. 5 is 2.44 eV, indicating that adding the Si atoms to the interface structure of Fig. 6 requires 1.22 eV/atom at full occupancy. Although the model of Fig. 6 has lower formation energy, the model of Fig. 5 is also attractive because there is a weak contrast in the experimental STEM images at the positions of the Si atoms in L3, which is better reproduced by Fig. 5. Thus it is possible that there is partial occupancy of the Si atom sites.

Figure 7 shows our best model of the Co-initiated interface with the same set of ball and stick models along [110] and [1$\bar{1}$0] and the corresponding STEM simulations and experimental images. The simulated and experimental images are in good agreement. In this model, the Mn has diffused past Co into layers from L1 through L4, with Co atoms in layer L5, and there is a Mn_2As-like structure in layers L1 and L2.

A model for the Co-initiated interface with Si in L3 was unstable under energy minimization. The formation energy for the Co-initiated model in Fig. 7 is −0.299 eV/atom.

B. Electronic and magnetic properties

The total density of states (DOS) for the Fig. 5 structure is shown in Fig. 8(a). The total DOS exhibits interface states at the Fermi level (E_F) in the minority band, so the interface does not have a gap in the minority spin band and is not half-metallic. The spin-polarization (P) at E_F is 0.77. Away from E_F the number of states in the minority band increases drastically, further reducing the spin polarization. The DOS of CMS/GaAs (001) with an ideal abrupt MnSi/As termination is shown as the shaded curve. It preserves the gap in the minority band.

The layer-by-layer local DOS (LDOS) of the Fig. 5 interface is shown in Fig. 8(b). The interface states arise from all but one layer, the L6 MnAs layer. There is a complex hybridization due to the presence of Si in layer L3. The minority conduction-band edge approaches the Fermi energy due to hybridization of Co d states (L5) and As s,p states (L4). The minority valence-band edge is shifted towards the Fermi level compared to the ideal abrupt model due to the hybridization of Mn d states in L2 and Si s,p states in L3. The LDOS of Mn in L3 suggests charge transfer from this Mn atom to Si in L3.

Table I reports the spin polarization of only the (s,p)-character states ($P_{s,p}$), which is a more relevant quantity than the total spin polarization for transport properties [57], and magnetic moment, m, for every atom in the interface. The $P_{s,p}$ values show that interfacial states appear in all layers of the complex interface structure, and the $P_{s,p}$ value is particularly low for Si in L3 and for As in L2 and L4. The magnetic moment

TABLE I. The calculated (s,p)-character spin polarization, $P_{s,p}$, and the magnetic moment, m (μ_B), of atoms at the interface for all three DFT models.

Descriptions	Interface layers	$P_{s,p}$		Magnetic moment (μ_B)	
		Atom 1	Atom 2	Atom 1	Atom 2
MnSi-initiated model (Fig. 5)	L6: Mn As	0.85	0.91	3.165	0.017
	L5: Co Co	0.74	0.58	1.07	1.033
	L4: Mn As	0.5	0.38	2.842	−0.001
	L3: Mn Si	0.70	0.34	1.218	−0.11
	L2: Mn As	0.76	0.47	2.551	−0.01
	L1: Ga	0.46	–	−0.019	–
MnSi-initiated model (Fig. 6)	L6: Mn As	0.98	0.98	3.231	0.019
	L5: Co Co	0.88	0.93	1.15	1.009
	L4: Mn As	0.86	0.88	2.999	0.017
	L3: Mn	0.52	–	−0.936	–
	L2: Mn As	0.24	−0.16	3.594	0.022
	L1: Ga	−0.11	–	0.028	–
Co-initiated model (Fig. 7)	L6: Mn As	0.97	0.95	3.228	0.017
	L5: CoCo	0.75	0.92	1.124	1.017
	L4: Mn As	0.92	0.90	3.178	0.022
	L3: Mn	0.33	–	−2.121	–
	L2: Mn As	0.52	0.67	2.567	−0.064
	L1: Mn	0.35	–	2.773	–

of Mn in L3 is $+1.218\,\mu_B$, and the moment of Si in L3 is $-0.11\,\mu_B$, indicating weak antiferromagnetic coupling.

The total DOS and layer-by-layer partial DOS for the alternate Mn/MnSi-initiated interface in Fig. 6 are shown in Fig. 9. There is no gap at E_F and the spin polarization is $P = 0.6$, although there is a finite gap of 0.07 eV, shifted below E_F. The LDOS in Fig. 9(b) shows that the major cause for interface states at E_F for minority spin bands is hybridization between L2 - MnAs and L1 - Ga. Inspection of individual atom-projected DOS of Mn d character and the (s,p) characters of Ga, and As suggest a strong hybridization between these orbitals in layers L1 and L2. Unlike the ideal, half-metallic, abrupt SiMn/As termination [39], in which the last layer of Co in the CMS is shielded from As by interfacial MnSi, in this model, the Co layer at L5 is adjacent to As in both layers L4 and L6, with As at L4 being the nearest neighbor to Co at L5. As a result, Co hybridizes with As such that the minority d band of Co shifts to lower energy, and the Co band gap at the minority band shrinks, similar to the DOS characteristics of Co_2MnAs [58]. As shown by the $P_{s,p}$ values in Table I, the major source of the interface states are layers L1 and L2, and to an extent layer L3. The magnetic moment of Mn atom in L2 is significantly larger ($3.594\,\mu_B$) than that of a Mn atom in bulk CMS, which is $\sim 2.997\,\mu_B$. The moments of L1-Ga and L2-As also are significantly enhanced compared to bulk GaAs. The magnetic moment of Mn atom in L3 is antiferromagnetically aligned to the moments of MnAs in layers L4 and L2. The magnetic moments and the spin polarization in CoCo, and MnAs in layers L4 and L5 behave similarly to those in bulk-Co_2MnAs [41], except for a small loss in spin polarization.

The same total DOS and layer-by-layer partial DOS for the Co-initiated interface model in Fig. 7 are shown in Fig. 10(a) and 10(b), respectively. The total DOS again shows interface states and loss of half metallicity, leading to a spin polarization at E_F of 0.52, less than the Mn/MnSi-initiated model (Figure 5). The ideal abrupt Co/As model (shaded curve) does not preserve half-metallicity. The layer-by-layer DOS shows that the main source of interface states is the Mn_2As-like structure in layers L1 and L2. The LDOS plots of layers L3-L6 have gaps near the Fermi level and very high spin-polarization. The $P_{s,p}$ is very low for atoms in layers L1, L2, and L3, as shown in Table I, suggesting that the interface states that destroy the half-metallicity arise from atoms in these layers. The major difference in magnetic ordering in the Co-initiated interface compared to the Mn/MnSi-initiated interface is the moment of Mn at L3. In the Mn/MnSi-initiated interface, all the Mn have positive magnetization and ferromagnetic coupling from layer to layer. In the Co-initiated interface, the Mn in L3 has a magnetic moment of $-2.121\,\mu_B$ and is antiferromagnetically ordered to the moments in layers L2 and L4. This magnetic moment behavior is consistent with that of bulk Mn_2As, which is antiferromagnetic [59].

The forward J-V characteristics of the three interfaces at temperature $T = 30$ K are shown in Fig. 11(a). The most significant aspect of these data is the trend in the tunneling current as the initiation changes from Co to MnSi to Mn. The current density for a given bias voltage decreases by over an order or magnitude, so that the Schottky barrier becomes more rectifying. In contrast, the nonlocal spin valve signal (for the same bias conditions at 20 K) *increases* as the initial layer is changed from Co to Mn, as shown in Fig. 11(b). The signal of interest is the difference in nonlocal voltage between the parallel and antiparallel states of the two electrodes, which is approximately $150\,\mu$V for the Co-initiated sample and over $600\,\mu$V for the Mn-intiated sample. By comparing with Fe-based devices with comparable channel doping [60], the spin accumulation in the Mn-terminated case is of order 50%. These trends are consistent with the electronic structure calculations discussed above, for which the highest polarizations were found for the Mn-terminated interfaces. However, the noise is

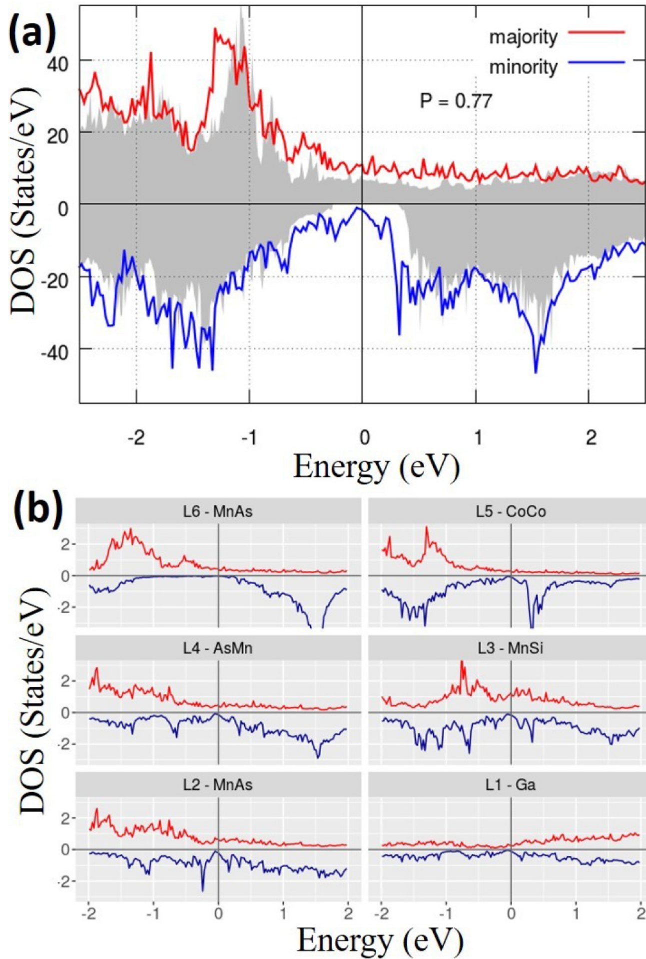

FIG. 8. (a) Total DOS of the periodic supercell structure for the MnSi-initiated model with Si shown in Fig. 5. The total DOS for CMS/GaAs(001) with ideal abrupt SiMn/As termination is shown in the shaded portion. (b) Layer-by-layer LDOS at the interface for the same model. The DOS of L1-Ga are multiplied by a factor of 5 with respect to other DOS plot for comparison.

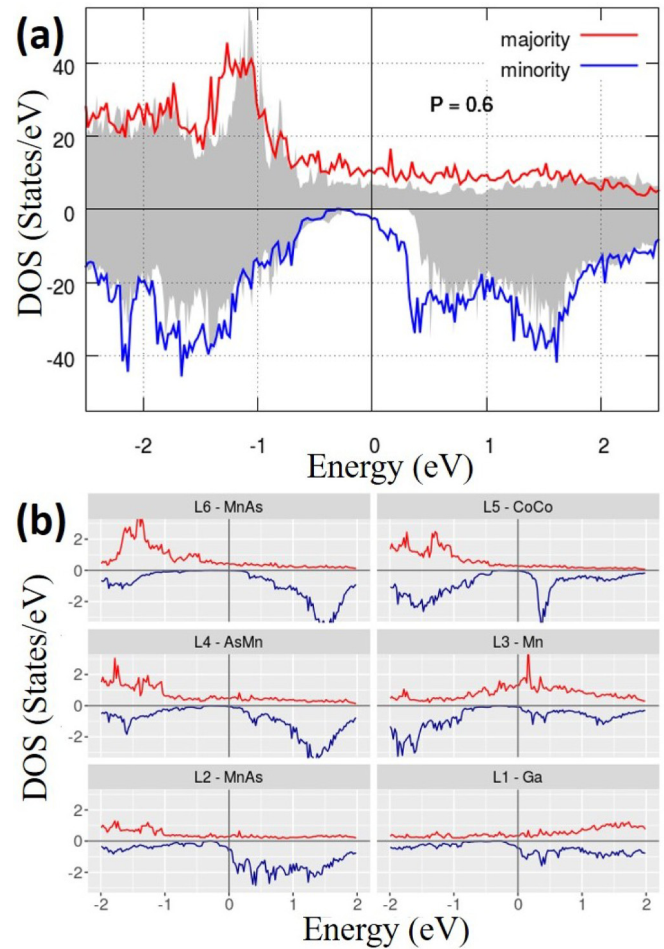

FIG. 9. (a) Total DOS of the DFT-model for the MnSi-initiated model without Si at L3 shown in Fig. 6. The total DOS for ideal abrupt SiMn interface is shown in the shaded portion. (b) The layer-by-layer LDOS at the interface for the same model.

also largest for the Mn-terminated interface, which prevented any quantitative analysis of these data over a significant range of bias and temperature. In fact, although Co_2MnSi/GaAs spin valves have shown the largest nonlocal spin-valve *voltages*, the diffusion of Mn into GaAs, which we have confirmed using secondary ion mass spectroscopy, appears to lead to both more rectifying behavior and an associated increase in noise.

C. Discussion

Two straightforward conclusions can be drawn from our results. The first is that simple, abrupt interfaces that are the easiest to create on the computer [39,41] are much more difficult to create in the real world. These computational models often predict half metallicity for ideal interfaces. For example, Ghaderi *et al.* [39] have shown that for the ideal abrupt SiMn/As termination that retains half-metallicity, the band edges around the minority gap are dominated by orbitals of As *p* character and of Mn *d* character. The first Co layer in the CMS is then screened from the interfacial As layer by a layer of MnSi. Previous theoretical studies have shown that MnSi-terminated (001) [41] and As-terminated (001) surfaces [31] are typically most stable for CMS and GaAs, respectively. Picozzi *et al.* studied the density of states for Co_2MnGe/GaAs interface as a function of different atomic termination by using first-principles calculation and showed the loss of half-metallicity at the interface in all type of atomic terminations [61]. Real interfaces in the CMS/GaAs system are complex, multilayer structures with significant interlayer mixing. In our model for a MnSi-initiated interface, half of the first neighbors of the MnSi interface layer (L3) are substituted by nonmagnetic As atoms coming from the GaAs layer. Those As atoms are next to the layer of Co atoms, and their nearest neighbors are both Mn and Si. The surface As is bonded to the substituted Mn below it due to Mn in-diffusion. This atomic arrangement significantly changes the interfacial structure and thereby the magnetic and electronic properties. It creates interface states which destroy the half-metallicity, and the combination of Mn in GaAs can readily result in antiferromagnetically coupled interfacial Mn.

The second conclusion is that even MBE growth at the fairly low temperature of 270 °C needed for good epitaxial growth is still too high to kinetically trap desirable interface

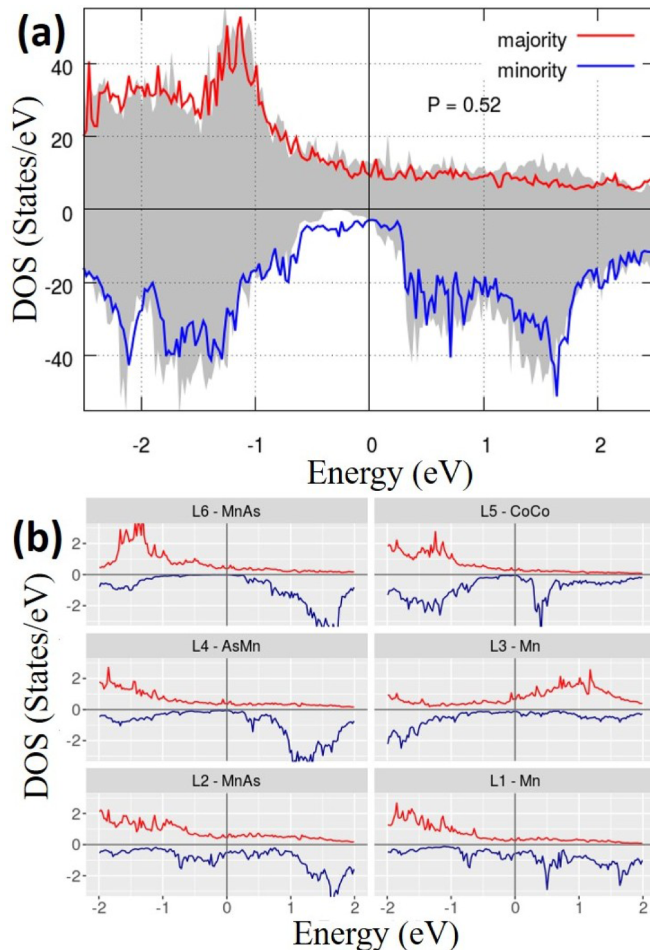

FIG. 10. (a) Total DOS of the DFT-model for the Co-initiated interface model in Fig. 7. The total DOS for CMS/GaAs(001) with Co/As ideal interface is shown in the shaded portion. (b) Layer-by-layer LDOS at the interface for the same model.

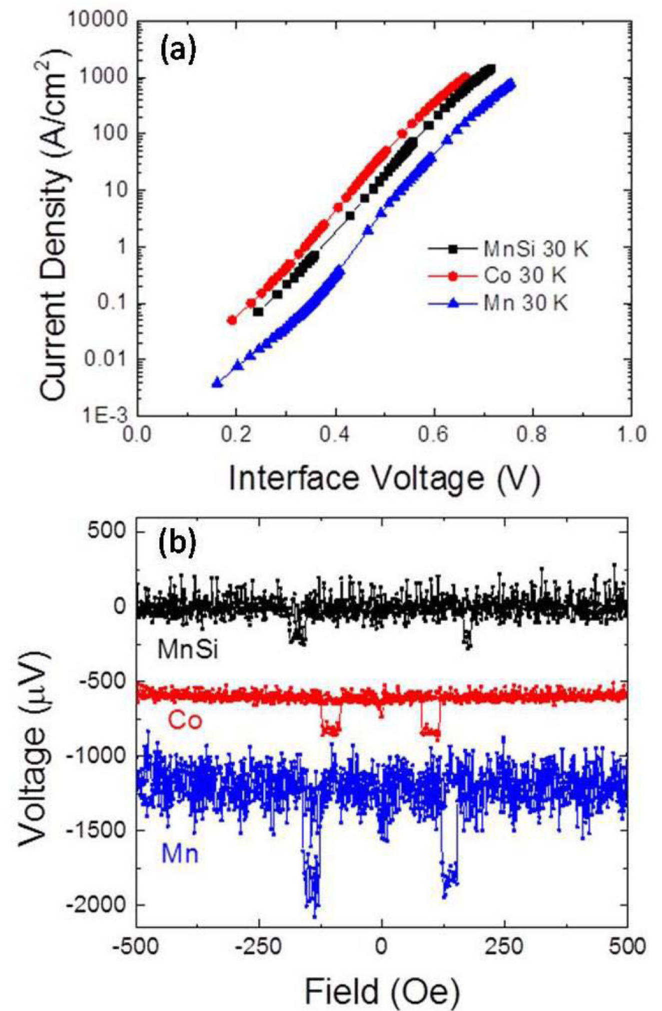

FIG. 11. (a) Forward current-voltage characteristics for the Co, MnSi, and Mn-initiated interfaces. The device structures are based on the graded Schottky barriers described in Ref. [28]. The same doping profile is used in all three samples. (b) Lateral spin valve signals for devices with the three types of interfaces obtained at 20 K with an injection current of 2.0 mA and a detector bias current of 0.5 mA. The nominal dimensions of the spin valve contacts were 5 μm × 50 μm, and the separation was 10 μm.

terminations in CMS/GaAs. Several reconstructions of the (001) GaAs surface are possible depending on the preparation conditions such as substrate temperature, the partial pressure of As and the availability of Mn adatoms. Mn atoms prefer to incorporate into interstitial sites in the moderate As rich $(2 \times 2)\beta$, Ga-rich (6×2) and $(2 \times 2)\beta$ reconstructed GaAs surface whereas substitutional sites are favored in As-rich $c(4 \times 4)$ reconstructed surface [62,63]. The issues related to interfacial intermixing of the atomic species and formation of secondary interfacial phases like Mn_2As and MnGa has been reported [30,64]. Singh *et al.* studied the CMS film on Ga-rich (4×2) GaAs (001) surface. The formation of Mn-As region at the interface was attributed to the diffusion of Mn into the GaAs [64]. The studies presented here are focused on only the As-rich reconstructions and we try to determine if the interfacial ordering in Co_2MnSi/GaAs heterostructures could be controlled or modified, how the interfacial ordering affects spin polarization, and how these factors affect the performance of lateral spin valve devices. While the Mn- and Co-initiated interfaces are different, both exhibit substantial Mn segregation. Elemental Mn is not thermodynamically stable in contact with GaAs and solid-state reactions of Mn on GaAs proceed via diffusion of Mn into the GaAs and the continued diffusion of Mn through a reacted interface [42]. Here, we show that both Mn in-diffusion and the As out-diffusion contribute to the formation of MnAs region and CMS/GaAs interface is always Mn-rich regardless of initiation sequence. This suggests that there is a strong driving force to form a Mn-GaAs type interface, and at the high substrate temperatures of 270 °C, there is enough energy for the Mn to bury under the Co layer to form a stable interface. It may be possible to make additional progress by control of Mn flux and temperature during the initial growth of the CMS layer, but it seems likely that some completely different method would be required to realize the abrupt terminations that are predicted to yield 100% interfacial spin polarization.

As shown in Fig. 11, spin injection through these interfaces has been observed [29] for each of the samples discussed in this paper. Although the interface is not 100% spin polarized, the spin valve signals are larger than those obtained for Fe

contacts [60,65], confirming a high degree of spin polarization (∼50% spin accumulation in the GaAs at low temperature). The implications of the interfacial structures described here for spin injection are, however, difficult to disentangle from other complicating factors. Most significantly, Mn diffuses a significant distance into the GaAs at low enough concentrations [66], so that the effective width of the Schottky tunnel barrier that is required for spin injection varies significantly among the three cases. This is confirmed by the current-voltage characteristics of devices fabricated from the three heterostructures, which become more rectifying as the initiation is varied from Co to MnSi to Mn [Fig. 11(a)], reflecting an increasing degree of compensation by Mn acceptors. Nevertheless, all three samples show nonlocal spin valve signals, with the highest values (for a fixed current density) observed for the Mn-terminated case [Fig. 11(b)].

A complete analysis of the polarization of the injected current has not been undertaken, but the values of the spin-signal for the Mn initiated sample imply a current spin polarization of the order of 50% at low temperature [28]. The differences between the spin-dependent transport properties of the Mn and MnSi-initiated samples are significant in light of the fact that our STEM and EELS measurements were not able to detect a significant difference in the interfaces. In addition to possible differences between the interfaces, it should also be noted that the first several layers of CMS are imperfect showing primarily a B_2 type of disorder indicating mixing of the Mn and Si.

IV. SUMMARY AND CONCLUSIONS

We studied CMS/GaAs(100) c(4 × 4) interfaces as function of the composition of the first CMS layer deposited, which was MnSi, Mn, and Co. We derived interface structural models for the CMS/GaAs interfaces using atomically resolved STEM and EELS. These models show that Mn segregation strongly influences the interface structures and thereby the interface spin polarization. Theory suggests that Mn- and MnSi-initiated interfaces have a higher degree of spin polarization than the Co-initiated case, although half-metallicity is lost for all three. DFT calculations for the MnSi/Mn-initiated structures suggest the reduced magnetic moment of Mn and weak antiferromagnetic coupling of Si in the subinterface layers. The Co-initiated interface has interface states arising from Mn_2As-like layers with antiferromagnetic coupling between Mn in different layers. Our experimental results combined with the theoretical investigations enable us to better interpret the interfaces of Heusler/semiconductor at the atomic scale, which will be helpful in engineering the interface for spintronic applications.

ACKNOWLEDGMENTS

This work was supported in part by C-SPIN, one of the six centers of STARnet, a Semiconductor Research Corporation program, sponsored by MARCO and DARPA. Electron microscopy used facilities supported by the UW-Madison Materials Research Science and Engineering Center (DMR-1121288). STEM-EELS was performed in the Characterization Facility of the University of Minnesota, which receives partial support from the NSF through the MRSEC. *Ab initio* DFT calculations were made possible in part by a grant of high performance computing resources and technical support from the Alabama Supercomputer Authority.

[1] I. Žutić, J. Fabian, and S. Das Sarma, Rev. Mod. Phys. **76**, 323 (2004).
[2] S. A. Wolf, D. D. Awschalom, R. A. Buhrman, J. M. Daughton, S. von Molnár, M. L. Roukes, A. Y. Chtchelkanova, and D. M. Treger, Science **294**, 1488 (2001).
[3] G. A. Prinz, Science **282**, 1660 (1998).
[4] Y. Sakuraba, M. Hattori, M. Oogane, Y. Ando, H. Kato, A. Sakuma, T. Miyazaki, and H. Kubota, Appl. Phys. Lett. **88**, 192508 (2006).
[5] H. Liu, Y. Honda, T. Taira, K. Matsuda, M. Arita, T. Uemura, and M. Yamamoto, Appl. Phys. Lett. **101**, 132418 (2012).
[6] Y. Sakuraba, K. Izumi, T. Iwase, S. Bosu, K. Saito, K. Takanashi, Y. Miura, K. Futatsukawa, K. Abe, and M. Shirai, Phys. Rev. B **82**, 094444 (2010).
[7] J. Sato, M. Oogane, H. Naganuma, and Y. Ando, Appl. Phys. Express **4**, 113005 (2011).
[8] M. J. Carey, S. Maat, S. Chandrashekariaih, J. A. Katine, W. Chen, B. York, and J. R. Childress, J. Appl. Phys. **109**, 093912 (2011).
[9] R. A. de Groot, F. M. Mueller, P. G. van Engen, and K. H. J. Buschow, Phys. Rev. Lett. **50**, 2024 (1983).
[10] B. Balke, S. Wurmehl, G. H. Fecher, C. Felser, and J. Kübler, Sci. Technol. Adv. Mater. **9**, 014102 (2008).
[11] S. Fujii, S. Sugimura, Ishida, and S. Asano, J. Phys. Condens. Matter **2**, 8583 (1990).
[12] I. Galanakis, P. H. Dederichs, and N. Papanikolaou, Phys. Rev. B **66**, 174429 (2002).
[13] I. Galanakis, P. H. Dederichs, and N. Papanikolaou, Phys. Rev. B **66**, 134428 (2002).
[14] J. A. Caballero, A. C. Reilly, Y. Hao, J. Bass, W. P. Pratt, F. Petroff, and J. R. Childress, J. Magn. Magn. Mater. **198–199**, 55 (1999).
[15] T. Akiho, J. Shan, H. X. Liu, K. I. Matsuda, M. Yamamoto, and T. Uemura, Phys. Rev. B **87**, 235205 (2013).
[16] S. Picozzi, A. Continenza, and A. J. Freeman, Phys. Rev. B **66**, 094421 (2002).
[17] S. Ishida, S. Fujii, S. Kashiwagi, and S. Asano, J. Phys. Soc. Jpn. **64**, 2152 (1995).
[18] P. J. Brown, K. U. Neumann, P. J. Webster, and K. R. A. Ziebeck, J. Phys. Condens. Matter **12**, 1827 (2000).
[19] L. Ritchie, G. Xiao, Y. Ji, T. Y. Chen, C. L. Chien, M. Zhang, J. Chen, Z. Liu, G. Wu, and X. X. Zhang, Phys. Rev. B **68**, 104430 (2003).
[20] Y. Sakuraba, J. Nakata, M. Oogane, H. Kubota, Y. Ando, A. Sakuma, and T. Miyazaki, Jpn. J. Appl. Phys. **44**, L1100 (2005).
[21] L. J. Singh, Z. H. Barber, Y. Miyoshi, Y. Bugoslavsky, W. R. Branford, and L. F. Cohen, Appl. Phys. Lett. **84**, 2367 (2004).
[22] S. Kämmerer, A. Thomas, A. Hütten, and G. Reiss, Appl. Phys. Lett. **85**, 79 (2004).

[23] M. Jourdan, J. Minár, J. Braun, A. Kronenberg, S. Chadov, B. Balke, A. Gloskovskii, M. Kolbe, H. J. Elmers, G. Schönhense, H. Ebert, C. Felser, and M. Kläui, Nat. Commun. **5**, 3974 (2014).
[24] W. H. Wang, M. Przybylski, W. Kuch, L. I. Chelaru, J. Wang, Y. F. Lu, J. Barthel, H. L. Meyerheim, and J. Kirschner, Phys. Rev. B **71**, 144416 (2005).
[25] S. Andrieu, A. Neggache, T. Hauet, T. Devolder, A. Hallal, M. Chshiev, A. M. Bataille, P. Le Fèvre, and F. Bertran, Phys. Rev. B **93**, 094417 (2016).
[26] N. J. Harmon, T. A. Peterson, C. C. Geppert, S. J. Patel, C. J. Palmstrøm, P. A. Crowell, and M. E. Flatte, Phys. Rev. B **92**, 140201(R) (2015).
[27] C. Liu, S. J. Patel, T. A. Peterson, C. C. Geppert, K. D. Christie, G. Stecklein, C. J. Palmstrøm, and P. A. Crowell, Nat. Commun. **7**, 10296 (2016).
[28] T. A. Peterson, S. J. Patel, C. C. Geppert, K. D. Christie, A. Rath, D. Pennachio, M. E. Flatté, P. M. Voyles, C. J. Palmstrøm, and P. A. Crowell, Phys. Rev. B **94**, 235309 (2016).
[29] C. J. Palmstrøm, Prog. Cryst. Growth Charact. Mater. **62**, 371 (2016).
[30] J. L. Hilton, B. D. Schultz, and C. J. Palmstrøm, J. Appl. Phys. **102**, 063513 (2007).
[31] Z. Yang, K. Zhang, S. Ke, and X. Xie, Phys. Rev. B **56**, 6727 (1997).
[32] S. Picozzi, A. Continenza, and A. J. Freeman, Phys. Rev. B **69**, 094423 (2004).
[33] S. Picozzi, A. Continenza, and A. J. Freeman, J. Phys. Chem. Solids **64**, 1697 (2003).
[34] L. Y. Chen, S. F. Wang, Y. Zhang, J. M. Zhang, and K. W. Xu, Thin Solid Films **519**, 4400 (2011).
[35] Y. Miura, K. Nagao, and M. Shirai, Phys. Rev. B **69**, 144413 (2004).
[36] G.-f. Li, Y. Honda, H.-x. Liu, K. Matsuda, Phys. Rev. B **89**, 014428 (2014).
[37] M. Yamamoto, T. Ishikawa, T. Taira, G. Li, K. Matsuda, and T. Uemura, J. Phys. Condens. Matter **22**, 164212 (2010).
[38] T. Ishikawa, H.-X. Liu, T. Taira, K. Matsuda, T. Uemura, and M. Yamamoto, Appl. Phys. Lett. **95**, 232512 (2009).
[39] N. Ghaderi, S. J. Hashemifar, H. Akbarzadeh, and M. Peressi, J. Appl. Phys. **102**, 074306 (2007).
[40] Z. Nedelkoski, P. J. Hasnip, A. M. Sanchez, B. Kuerbanjiang, E. Higgins, M. Oogane, A. Hirohata, G. R. Bell, and V. K. Lazarov, Appl. Phys. Lett. **107**, 212404 (2015).
[41] S. J. Hashemifar, P. Kratzer, and M. Scheffler, Phys. Rev. Lett. **94**, 096402 (2005).
[42] J. L. Hilton, B. D. Schultz, S. McKernan, S. M. Spanton, M. M. R. Evans, and C. J. Palmstrøm, J. Vac. Sci. Technol. B **23**, 1752 (2005).
[43] A. Ohtake, Surf. Sci. Rep. **63**, 295 (2008).
[44] R. F. Egerton, *Electron Energy-Loss Spectroscopy in the Electron Microscope* (Springer US, Boston, MA, 2011).
[45] F. Shi, Ph.D Dissertation, University of Wisconsin-Madison, 2013.
[46] P. Hohenberg and W. Kohn, Phys. Rev. **136**, B864 (1964).
[47] J. P. Perdew, K. Burke, and M. Ernzerhof, Phys. Rev. Lett. **77**, 3865 (1996).
[48] G. Kresse and J. Hafner, Phys. Rev. B **47**, 558 (1993).
[49] G. Kresse and J. Hafner, Phys. Rev. B **49**, 14251 (1994).
[50] G. Kresse and J. Furthmüller, Comput. Mater. Sci. **6**, 15 (1996).
[51] G. Kresse and J. Furthmüller, Phys. Rev. B **54**, 11169 (1996).
[52] W. Press, S. Teukolsky, W. Vetterling, and B. Flannery, *Numerical Recipes: The Art of Scientific Computing* (Cambridge University Press, Cambridge, 1989).
[53] J. D. Pack and H. J. Monkhorst, Phys. Rev. B **16**, 1748 (1977).
[54] E. J. Kirkland, *Advanced Computing in Electron Microscopy* (Springer US, Boston, MA, 2010).
[55] A. B. Yankovich, B. Berkels, W. Dahmen, P. Binev, S. I. Sanchez, S. A. Bradley, A. Li, I. Szlufarska, and P. M. Voyles, Nat. Commun. **5**, 4155 (2014).
[56] A. Kohn, V. K. Lazarov, L. J. Singh, Z. H. Barber, and A. K. Petford-Long, J. Appl. Phys. **101**, 023915 (2007).
[57] K. Nagao, Y. Miura, and M. Shirai, Phys. Rev. B **73**, 104447 (2006).
[58] W. Butler, J. Romero, and K. Munira, Http://heusleralloys.mint.ua.edu/ (2016).
[59] K. Shirakawa and H. Ido, J. Phys. Soc. Japan **40**, 666 (1976).
[60] X. Lou, C. Adelmann, S. A. Crooker, E. S. Garlid, J. Zhang, K. S. M. Reddy, S. D. Flexner, C. J. Palmstrøm, and P. A. Crowell, Nat. Phys. **3**, 197 (2007).
[61] S. Picozzi and A. J. Freeman, J. Phys.: Condens. Matter **19**, 315215 (2007).
[62] A. Ohtake, A. Hagiwara, and J. Nakamura, Phys. Rev. B **87**, 165301 (2013).
[63] A. Ohtake, A. Hagiwara, K. Okukita, K. Funatsuki, and J. Nakamura, J. Phys. Chem. C **120**, 6050 (2016).
[64] L. J. Singh, Z. H. Barber, A. Kohn, A. K. Petford-Long, Y. Miyoshi, Y. Bugoslavsky, and L. F. Cohen, J. Appl. Phys. **99**, 013904 (2006).
[65] M. K. Chan, Q. O. Hu, J. Zhang, T. Kondo, C. J. Palmstrøm, and P. A. Crowell, Phys. Rev. B **80**, 161206(R) (2009).
[66] D. C. Look and G. S. Pomrenke, J. Appl. Phys. **54**, 3249 (1983).